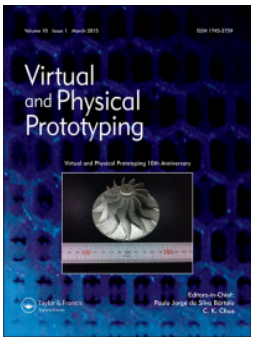

Virtual and Physical Prototyping

ISSN: 1745-2759 (Print) 1745-2767 (Online) Journal homepage: www.tandfonline.com/journals/nvpp20

Improving component dimensional accuracy in electron beam powder bed fusion by addressing nonlinear deformations with 3D compensation strategies

Chen Wang, Chen-Nan Sun, Lei Zhang, Stefanie Feih & Pan Wang

To cite this article: Chen Wang, Chen-Nan Sun, Lei Zhang, Stefanie Feih & Pan Wang (2024) Improving component dimensional accuracy in electron beam powder bed fusion by addressing nonlinear deformations with 3D compensation strategies, Virtual and Physical Prototyping, 19:1, e2430319, DOI: 10.1080/17452759.2024.2430319

To link to this article: https://doi.org/10.1080/17452759.2024.2430319

Published online: 04 Dec 2024.

VIRTUAL AND PHYSICAL PROTOTYPING
2024, VOL. 19, NO. 1, e2430319 (19 pages)
https://doi.org/10.1080/17452759.2024.2430319

Taylor & Francis
Taylor & Francis Group

OPEN ACCESS Check for updates

Improving component dimensional accuracy in electron beam powder bed fusion by addressing nonlinear deformations with 3D compensation strategies

Chen Wang [a], Chen-Nan Sun [a], Lei Zhang [a,b,c], Stefanie Feih [a,d] and Pan Wang [a]

[a]Singapore Institute of Manufacturing Technology (SIMTech), Agency for Science, Technology and Research (A*STAR), Singapore, Republic of Singapore; [b]Meta Robotics Institute, Shanghai Jiao Tong University, Shanghai, People's Republic of China; [c]State Key Laboratory of Mechanical System and Vibration, Shanghai Jiao Tong University, Shanghai, People's Republic of China; [d]School of Engineering and Built Environment, Griffith University, Southport, Australia

ABSTRACT

Electron beam powder bed fusion (EB-PBF) is effective for producing complex geometrical components with minimal residual stress because of elevated powder bed temperatures; however, it faces challenges in achieving dimensional accuracy due to nonlinear shrinkage. We systematically investigated the thermal shrinkage behaviour of large-scale EB-PBF components and developed 3D nonlinear compensation strategies. A thermal-mechanical model was developed to simulate residual stress and deformation during printing and cooling, revealing that nonlinear shrinkage is linked to thermal history, stress distribution, and material properties. The proposed method improved dimensional accuracy, reducing maximum errors from 1.81 mm to 0.16 mm, meeting industrial tolerances for components sized 77 × 48 × 326 mm. Hereafter, we developed a comprehensive digital workflow encompassing topology optimisation and compensation, validated through a case study on a topology-optimised satellite component. This approach enhances manufacturing precision and significantly reduces trial-and-error iterations in product design, resulting in substantial time and cost savings.

ARTICLE HISTORY
Received 3 October 2024
Accepted 12 November 2024

KEYWORDS
Additive manufacturing; electron beam melting; distortion compensation; thermal shrinkage; printing accuracy; thermal-mechanical modelling

1. Introduction

The global rise in demand for metal additive manufacturing (AM) to produce complicated engineering components is nowadays driving the growth of market size and cutting-edge research [1,2]. Industries, such as aerospace, healthcare, automobile, tools and moulds segment, consider AM as a key alternative to conventional manufacturing technologies since it enables freedom in design complexity and effectiveness of making near-net shape metallic components [3,4]. However, challenges like cost, quality, scalability, and geometric inaccuracy caused by thermal distortion or shrinkage in the layer-by-layer process hinder broader industry adoption [5]. Current solutions, such as iterative printing and rework, are time-consuming and costly, particularly for parts requiring high dimensional accuracy. Residual stress generated in the metal AM process is regarded as one of the root causes of part distortion [6–8]. The temperature gradient and the cool-down phase are two formation mechanisms of residual stress [7]. The former is associated with melt pool expansion, when powders are heated to melt, causing upward bulging. This expansion is constrained by the surrounding cooler material, creating residual stress. At elevated temperature, metal easily yields, converting thermal strain into plastic strain. The latter refers to shrinkage of each newly deposited layer when material cools, constrained by the previously deposited layer. This results in tensile stress in the newly deposited layer and compressive stress in the preceding layer. Among various metal AM processes, electron beam powder bed fusion (EB-PBF) process, based on metal powder and a high energy electron beam, can build parts with low residual stress [8] largely due to its advanced preheating capability and vacuum environment [9,10]. This has made EB-PBF widely adopted for manufacturing industrial components with decent as-printed accuracy and minimal need for supports [10].

Nevertheless, recent research reported that printing dimensional error of an EB-PBF part cannot be neglected nor precisely predicted, especially in truss, thin-wall and overhanging structures, with structural geometry,

CONTACT Pan Wang wangp@simtech.a-star.edu.sg Singapore Institute of Manufacturing Technology (SIMTech), Agency for Science, Technology and Research (A*STAR), 5 Cleantech Loop, Singapore 636732, Republic of Singapore

material properties and processing parameters playing an important and interacting role. Peng et al. [11] reported that geometrical discrepancy led to anisotropic mechanical behaviour of EB-PBF printed Gyroid scaffolds. Wang et al. [9] found heterogeneous and localised deformation behaviour of thin-wall structures with thicknesses of less than 2 mm. Chen et al. [12] examined thin-walled rectangular profiles, finding that deformation primarily occurred along the length, with the maximum deformation at the mid-point of the height. Ghaoui [13,14] and Cheng et al. [15] described thermal distortions of overhang structures, such as side loss and curling. Although these studies highlighted special shapes that caused undesired distortion, no specific rationale was revealed between deformation and residual stress. Zafar et al. [16] summarised key powder material properties affecting residual stress levels in the EB-PBF process. Dong et al. [17] numerically correlated T-6Al-4V part distortion with residual stress profile and heat accumulation. Franchitti et al. [18] stated that the dimensional accuracy of EB-PBF samples was affected by orientation and height position of the sample in the build chamber. Zhao et al. [19] reduced the plastic strain by using a proper layer rotation scanning strategy. Overall, current studies discussed the effects of heat source, supports, process parameters and material properties individually, but did not address the interactions between multiple thermal and mechanical factors. The complexity of part deformation was recently summarised as a stress-deformation-fracture-recovery process, making research expensive and impractical [20,21]. Hence, more efforts are needed to discover universal rules in prevalent industry circumstances, such as large-scale assembly and components, because the complex principles of EB-PBF distortion are not fully understood.

Two categories of solutions have been investigated to improve as-printed dimensional accuracy in metal AM. One approach is to minimise thermal shrinkage and distortion in metal AM by re-designing geometry, improving supporting structures and optimising processing parameters [9,22]. The other way is to compensate for shape distortion by scaling the part prior to being additively manufactured. Khrapov et al. [23] applied scaling factors to compensate for the distortion of EB-PBF Ti-6Al-4V gyroid scaffolds. Afazov et al. [10,24] developed an improved mathematical model for calculation displacement vectors for pre-distorting the geometry based on 3D optical scanning measurement data from Laser Powder Bed Fusion (L-PBF). Hong et al. [25] and Smith et al. [26] highlighted that linear scaling was not applicable for compensating geometrical defects of trusses in metal AM. Zhang et al. [27] developed a geometric compensation of L-PBF Ti-6Al-4V thin-walled parts by a data-driven algorithm from optical scanning data. Dalpadulo [28] studied distortion modelling and numerical compensation of PBF products considering design integration. These compensation methods have their respective advantages and disadvantages. Applying global scaling factors is easy and practical, but such an approach only accounts for total dimensions in a small length scale. Generally, mathematical methods based on in-advance measured data are developed specifically for one shape, which is not transferable to other geometries. Compensations based on finite-element (FE) analysis strongly rely on assumptions and constitutive laws of the coupled thermal-mechanical algorithm [29]. The models developed for L-PBF are not naturally applicable to the EB-PBF process and lacks experimental validations. Data-driven and artificial intelligence-assisted methods always lack high-quality training data [25]. Therefore, it is necessary to develop an operationally feasible compensation method based on general distortion rules of varying shapes in EB-PBF processes, considering the enhancement of both in-plane and out-of-plane assembly accuracy of large-scale industry components.

In this study, we aimed to address the part deformation and shrinkage issues encountered in the EB-PBF process. A series of experiments were conducted to investigate dimensional errors, validated by both small-scale test specimens and large-scale industrial components. Additionally, a thermal-mechanical model was applied to better understand the stress distributions obtained during printing. A 3D compensation method was proposed based on the experimental findings to mitigate shrinkage. This approach was subsequently integrated into a digital workflow from design for AM to full print, showcasing reduced product development cycles, increased printing accuracy and subsequent cost savings for industrial applications.

2. Materials and methods

2.1. EB-PBF process and materials

The EB-PBF equipment utilised, an Arcam A2X, has a build platform of 200 mm × 200 mm and a build height of 380 mm. It can operate at significantly higher powder bed temperatures than the L-PBF process at up to 1100 °C and is therefore well suited for printing long and slender components with minimal warpage. Ti-6Al-4V Grade 5 spherical powder with a size range from 45 to 106 µm [30] was used for all parts and demonstrators, with the printing parameters listed in Table 1. The EB-PBF process was carried out at a vacuum level of ~2×10^{-3} mBar, using high purity

Table 1. Printing parameters for Arcam A2X system.

Accelerating voltage (kV)	Preheating temperature (°C)	Speed function	Layer thickness (μm)	Line offset (μm)	Focus offset (mA)	Hatch depth (μm)
60	730	98	50	100	3	50

helium as a regulating gas to prevent powder charging. The base plate for the EB-PBF system consisted of a 10 mm thick stainless steel plate, which was heated to 730 °C prior to the process start. In each layer, the powder bed was preheated first using a defocused beam, so that the powder was at a semi-sintered stage. Following this, the electron beam performed a high-energy scan over the designated areas of each layer to fully melt the powder. This process selectively melts the powder according to the desired part geometry, layer by layer, to build up the component. After the melting step, the build platform is lowered, and a new layer of powder is spread across the previous layer, repeating the cycle until the component is completed. After finishing the build job and cooling the chamber to below 100 °C, the surrounding semi-sintered powder particles from the build were removed and recycled via a specialised Arcam Powder Recovery System (PRS). Here, the recovered powder from the PRS underwent sieving with a sieve mesh size of 150 μm. The recycled powder particles were added back to the hoppers for the next print.

2.2 EB-PBF beam samples and components

Figure 1(a) and (b) show sketches of beam samples designed to study part shrinkage in the rectangular coordinate system along orthogonal directions. The L-shaped beams were designed for studies along X and Y directions, with dimensions described in previous study [31]. The vertical beams were designed to be 142 mm in height to study shrinkage along the printing direction. The beam thickness was varied from 1, 2.5, 5, 10 to 20 mm, denoted as T1, T2.5, T5, T10 and T20, respectively. Arrays of measuring marks were designed with identical intervals of 25 mm. The positions of pilot holes with a diameter of 3 mm were measured after completing the EB-PBF process build. To eliminate any edge and build platform effects, the distortion was identified within a given gauge length so that the positions of each hole were normalised with regard to Hole 1. The gauge lengths were designed to be 100 mm for the vertical beams. Figure 1(a′) show respective photos of the as-printed L-shaped components. Figure (b′) show as-printed vertical beams with thickness of 1 mm (side view) and 2.5 mm (front view). In this study, we hypothesise that the overall thermal deformation of the part is a combination of local shrinkage along each coordinate direction.

Figure 1(c) shows demonstrators designed from a topology optimised bracket, which has a high fly-to-buy ratio and a large slenderness ratio. The part requires extensive bolt hole machining at three faces, with a high degree of alignment accuracy. Pilot holes with a diameter of 3 mm and an interval of 25 mm were printed along the part length, which was a total of 326 mm. Protrusion features around holes were reserved for post-processing. Overhang features were structurally optimised for assembly. As shown in Figure 1(c′), the print orientation of the long bracket must be upright, given the build platform dimension limits. In addition, upside-down orientations were proposed for comparison (marked as Orientation #1 and #2) to assess the potential orientation effect and floating supports effect. Finally, a systematic support optimisation was conducted to provide structural integrity, avoid unwanted distortion in the X and Y directions, and ensure uniform heat distribution between the parts during the EB-PBF printing process.

2.3. Coordinates measurement

Coordinate-measuring machine (CMM) is a traceable, well-established contact-based measurement technique that can be used to measure accessible external features. A Werth multi-functional CMM was used to measure centre positions of the discrete measuring marks on all components. Measurements were evaluated via scanning mode, as presented in Figure 2(a). The theoretical accuracy of the scanning mode is 2.15 μm; however, the exact value depends on the optical magnification and resolution. In this study, the tolerance of the CMM measurement was up to 90 μm, considering the typical rough surface (Ra = 31.7 ± 1.9 μm [32]) finish obtained from the EB-PBF. To measure the position of the pilot hole shown in Figure 2(b), individual points were captured from the edge based on image contrast to generate a circle. Corresponding coordinates of the circle centre were regarded as the centre position of the measuring marks. Obtaining centre coordinates of the measuring marks, the dimensional error was calculated as the coordinate difference between measured value and designed value. All measured coordinates were normalised with regard to Hole 1. The accumulated shrinkage was defined as the distance between each pilot hole and Hole 1. Measurements for each sample were carried

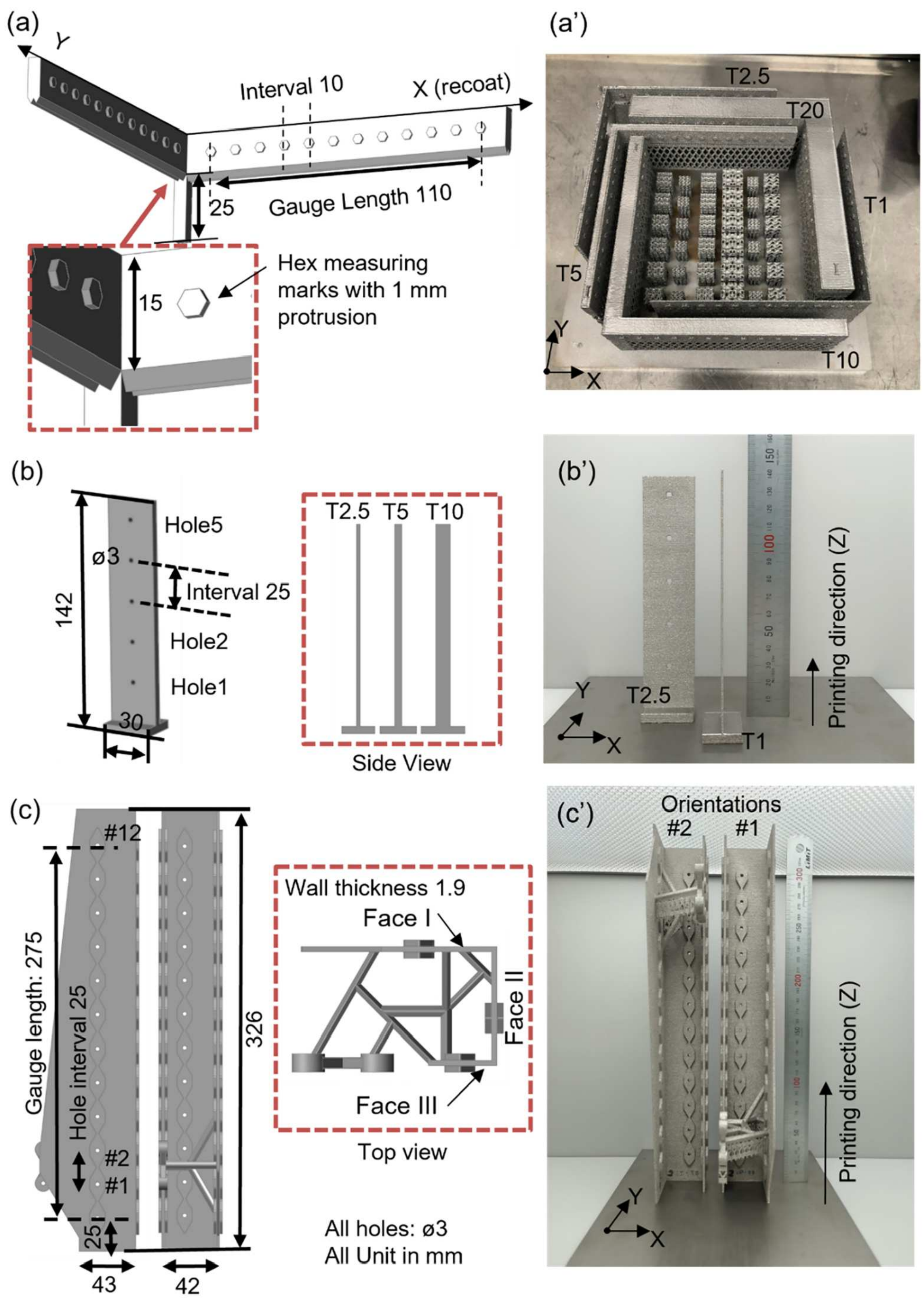

Figure 1. Sketch of (a) L-shaped beam with measurement marks, (b) vertical beam and (c) a long bracket component design with holes as measuring marks. (a'-c') Photos of as-printed specimens.

out twice for averaging. Due to the different points captured for fitting, the difference in centre positions between repeated tests was overall less than 20 μm.

2.4. Thermo-mechanical modelling for EB-PBF process

The EB-PBF processes of the demonstrators were modelled using a coupled thermal-mechanical method. The finite-element codes were commercially available in Altair® Inspire^{TM} Software (version 2022.1) with the Print3D module and Radioss solver [33]. The thermo-mechanical analysis enables the determination of a temperature field in the AM process, which is subsequently used to estimate thermal stresses and associated deformations through mechanical analysis. The basic and constitutive rules can be found in references [34–36].

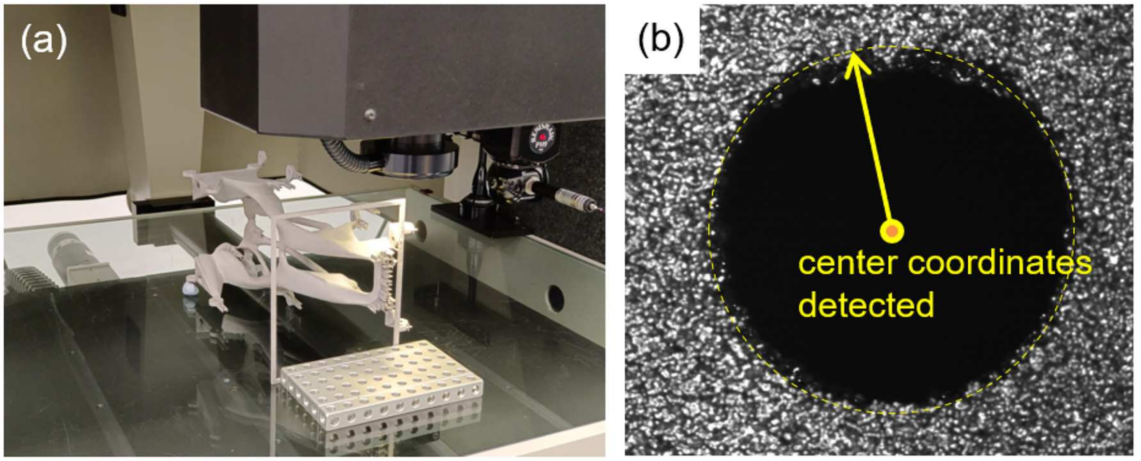

Figure 2. (a) Dimensional measurement in the scanning mode with CMM and (b) the fitting method for pilot-hole measuring marks.

Figure 3 shows the modelling steps and printing orientation set for the EB-PBF process simulation of the demonstrator. Printer parameters and material properties were set according to experiments, as shown in Table 2. Cubic voxel meshing was applied to the geometries and supporting structures. The element size was set as 0.6 mm, giving the minimum wall thickness of the demonstrator was 1.9 mm, while the element size for the base plate was 10 mm. The time step includes printing, cooling, support cutoff and spring-back, as per Figure 3. In the printing step, the voxel elements were activated layer by layer with heat energy applied. The thermal-mechanical iterations of activated elements were driven by thermal conductivity and emissivity, while the convection coefficient was assumed to be zero in the EB-PBF processes. Stress relaxation was considered in the spring-back step.

Material properties as a critical input for simulation and affect simulation results significantly when non-linear approaches are over-simplified [16,29]. However, various properties of AM powder materials are temperature-dependent and difficult to measure experimentally beyond room temperature (RT). Even Ti-6Al-4 V, which is widely studied in the literature as a powder and printed material, does not have a set of standardised material inputs that are universally accepted. In this study, several modifications of material properties were made based on default values from Altair Inspire

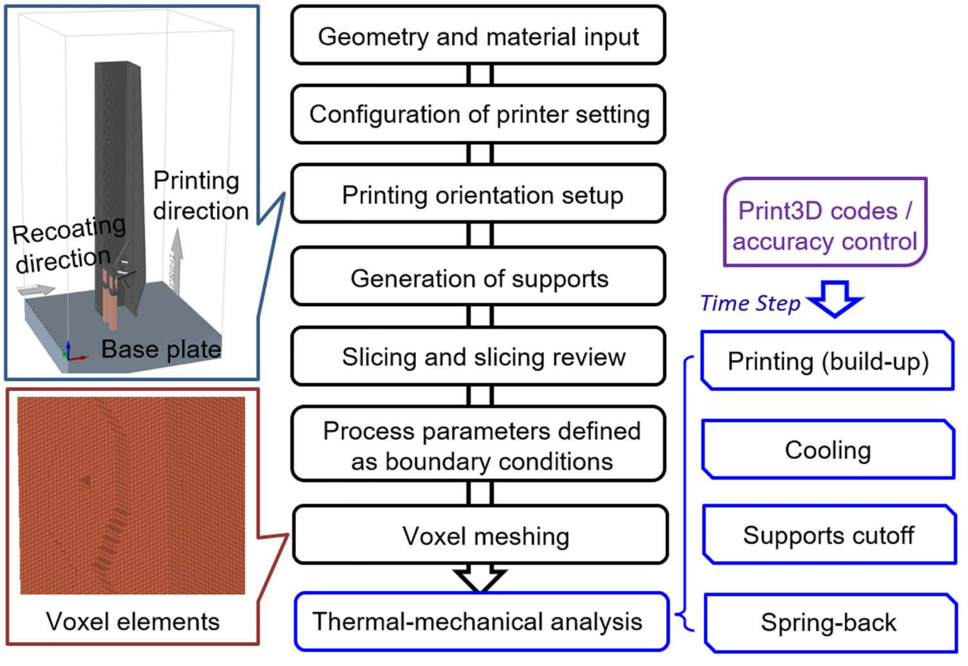

Figure 3. Simulation steps, model setup and mesh strategies for thermal-mechanical simulation of demonstrator.

Table 2. Printer parameters and printing process parameters used for EB-PBF process modelling.

Printer Parameters	Value	Process Parameters	Value
End path latency time [s]	1	Scanning speed [mm/s]	2440
Hatch width [mm]	0.2	Heat source power [W]	720
Hatch space [mm]	0.1	Powder layer thickness [mm]	0.05
Electron beam diameter [mm]	0.2	Heat absorption [%]	90
Recoating time [s]	8	Cooling time [hours]	8
Printing chamber size [mm3]	200 × 200 × 380	Base temperature [K]	1003

database [33] for Ti-6Al-4V material, as shown in Table 3. The modifications were selected using values commonly seen in Ansys database [37,38] and other references [39–41]. The parameter studies were conducted in a fast mode of the solver to identify material property input that significantly affect thermal deformation in EB-PBF process. The correlation of each material input data and resultant deformation were analysed to minimise the prediction error when comparing to experimental results. With the chosen input data (critical factors), an accurate mode of the solver was activated, so that the thermal and mechanical analyses were solved simultaneously at every time step. More output was therefore requested for calculation, increasing model accuracy and computational time. Therefore, Table 3 presents the choice of input data in this study, which was based on parameter studies and literature survey.

2.5. Dimensional compensation method

A compensation method was developed based on experimental observations along printing directions, assuming that the rules were consistent for the Ti-6Al-4V part printed with the given process parameters in Section 2.1. The basic algorithm, built-in MATLAB, is suitable to modify the coordinates of an STL object in the global coordinate system. Give Z direction as an example, we defined a unit vector $\vec{z}$. Given node O as the gauge length starting point with its Z coordinate, O_z, Z coordinate of any surface node P_i (i = 1 … n) from an STL file, we have the normalised Z position of node P_i as a vector

$$\vec{P_i} = (P_i - O_z)\vec{z}\,(i = 1\ldots n) \tag{1}$$

Hence, compensated vector

$$\vec{P_i}' = \eta\vec{P_i}\;(i = 1\ldots n), \tag{2}$$

or

$$\vec{P_i}' = \vec{P_i} - (\Delta d)\vec{z}'\;\;(i = 1\ldots n), \tag{3}$$

where η is a scaling factor calculated by ratio of total part height between the designed shape and shrunk shape after EB-PBF printing, and Δd is a dimensional error of each node between its position in the shrunk shape after the EB-PBF process and designed shape. In this study, the dimensional errors Δd was obtained from CMM measurement and process simulation, respectively. The compensated STL object is written to a new file in binary STL format for printing. Hence, three compensation methods were compared. In the first method, by applying Equation (2), a scaling factor assumes the dimensional error was distributed linearly along the part height. In the second method, Δd was obtained through interpolation of the coordinate difference of the pilot hole measured with CMM, as described in Section 2.3. After their respective nonlinear compensation, the parts were fabricated using the same EB-PBF process and measured with CMM again. In the third method, Δd was computed as the displacement of each node in the process simulation model. The compensated shape was analysed using the same material input and boundary conditions. Dimensional errors of compensated parts were hence compared as results of both experimental and numerical methods.

Table 3. Material properties input for thermal-mechanical modelling.

Material Properties	Value	Process Parameters	Value
Young's Modulus at RT [GPa]	109 [9]	Emissivity at preheating	0.7 [34,37]
Poisson's ratio	0.34 [33]	Convection Coefficient	0 [34,36]
Yield Strength at RT [MPa]	826 [9]	Specific Heat [J/(kg·K)]	553 [33]
Plastic Modulus [MPa]	350 [33]	Conductivity [W/(m·K)]	7.1 [38]
Plastic Exponent	0.3091 [33]	Coefficient of Thermal Expansion at RT [K^{-1}]	8.78E-6 [41]
Density [g/cm^3]	4.4 [39]	Melting Temperature [K]	1933 [38]

3. Results

3.1. Experimental results

According to Figure 1(a')–(c'), no significant out-of-plane distortion was observed for both thin-walled beam samples, and bracket components, even down to 1 mm wall thickness. This is primarily attributed to the in-situ heat treatment during the printing process. One of the key advantages of EB-PBF is its ability to maintain a high powder bed temperature, which effectively alleviates residual stresses during the solidification process [40]. In fact, the residual stress of as-built Ti-6Al-4V can be as low as 50 MPa [42]. As a result, the process enables the fabrication of thin-walled parts, particularly those with high aspect ratios. Figure 4(a) presents the

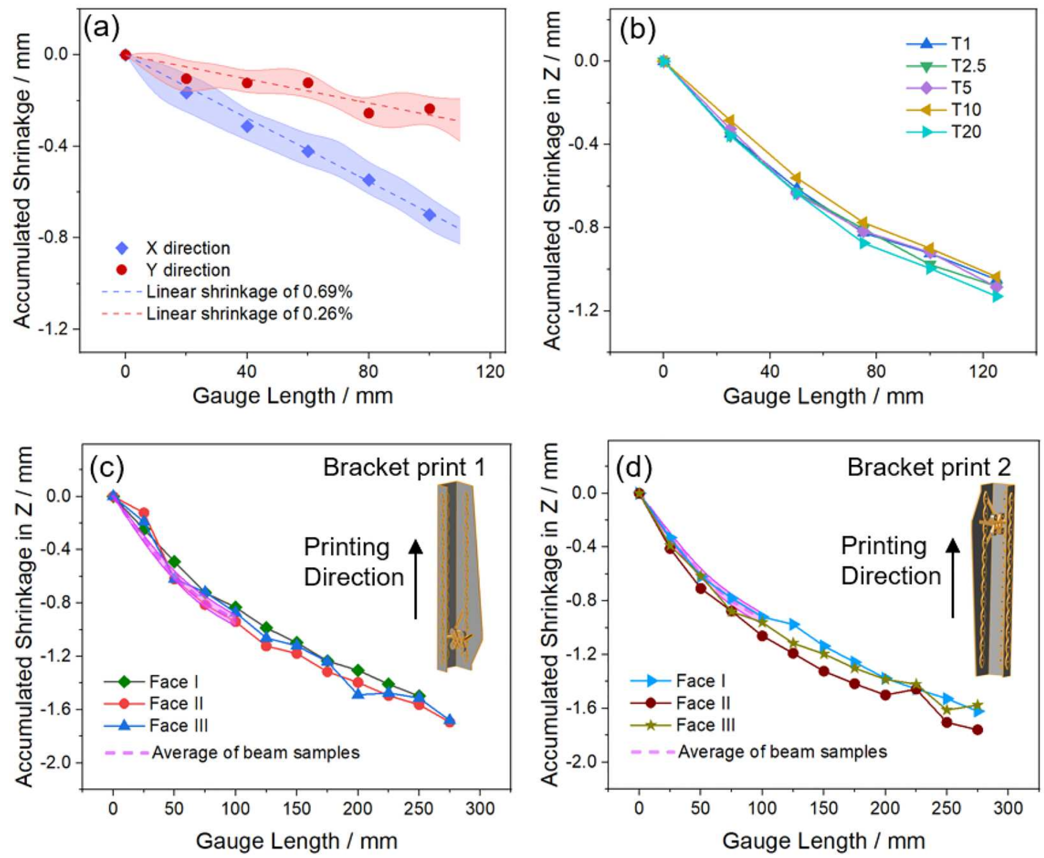

Figure 4. (a) Accumulated shrinkage measured from L-shaped beam samples along X and Y directions, respectively, and (b) comparison against cases of vertical beams along Z directions, as well as cases measured from bracket demonstrators printed in (c) original and (d) flipped printing orientations. The average values from the beam sample from (a) were inserted into (c) and (d) for comparison.

dimensional error of beam samples accumulated along the X and Y directions, respectively. The error was defined as a difference between the measured and designed centre coordinates of the prescribed marks. Within the gauge length of 100 mm, averaged total shrinkages of 0.69 % and 0.26 % were found along X and Y directions, respectively, which corresponded to magnitudes of 0.7 ± 0.07 and 0.24 ± 0.05 mm, respectively. Figure 4(b) shows the measured dimensional errors of the pilot hole positions from the vertical beam samples. The curves show shrinkage accumulation along the Z direction after the EB-PBF process since no obvious distortion or warpage had been seen in the X and Y directions for vertically printed beams. The trend was not linear as an approximate dimensional error of 0.61 mm was accumulated in the lower 50 mm height from the first measuring mark, while total shrinkage for the beam was approximately 0.93 mm by average within a gauge length of 100 mm. The results were consistent amongst samples with varying thicknesses, indicating no obvious thin-wall thickness effect in this study. Differences in magnitudes between samples were close to the measuring tolerance of around 0.09 mm. It was found that the deformation rule along the Z direction was nonlinear and, therefore, different from the shrinkage along the X and Y directions under the same process condition in our previous study [31]. In both X and Y directions, the overall trends were approximately linear, with R^2 values of 0.976 for the X direction and 0.997 for the Y direction in linear fittings, respectively. The shrinkage magnitudes in the X and the Y showed orthotropically discrepancy with smaller values than the shrinkage along the Z direction.

Figures 4(c) and (d) show the dimensional errors measured from pilot holes on three bracket surfaces of the 326 mm long industrial components. Compared with simple rectangular beams, the shrinkage of the brackets followed the same nonlinear trends for the two different printing orientation cases, with an averaging total shrinkage of 1.81 mm within gauge length. Deviations amongst the three faces were minor, while slightly larger shrinking magnitudes were observed on Face II. This is attributed to the fact that the holes on Face II were the furthest from the edge to dissipate heat. It was found that when the components were printed with original and reversed part orientations, the position of overhang features had no

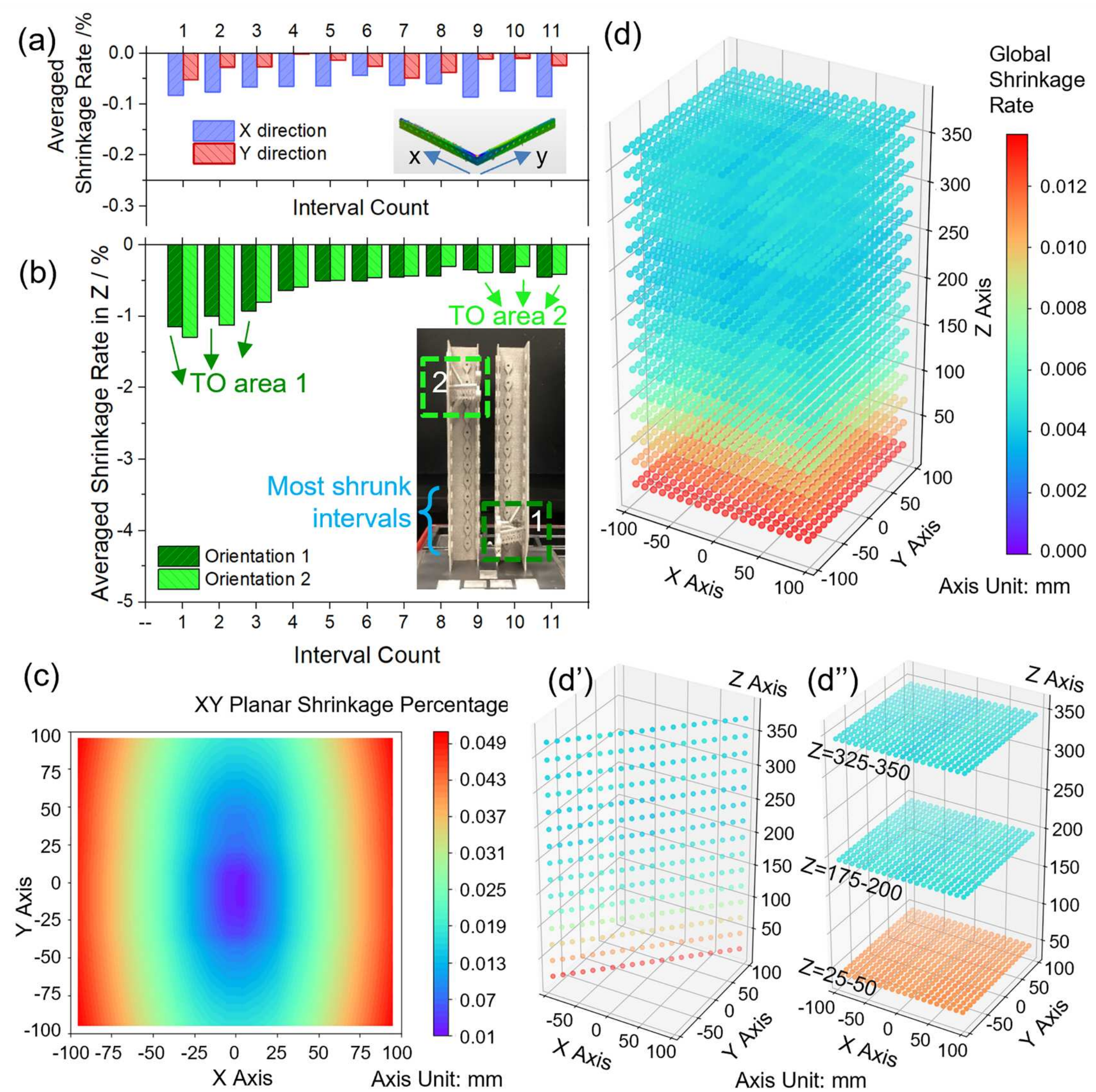

Figure 5. Averaging shrinkage rate of each interval between adjacent measuring marks along (a) X, Y and (b) Z direction measured from experiments. (c) Mapping of accumulated shrinkage percentage on XY plane considering the centre of the chamber as the origin point at measuring marks' height. (d) mapping of shrinkage rates of every voxel unit (10 mm ×10 mm × 25 mm) in the 3D space of the EB-PBF printing chamber, with (d') the distribution along the diagonal plane and (d'') XY planes at different heights.

apparent effect on the shrinkage of the whole bracket along the part height. Furthermore, the studies of beams and industrial components reflected that shrinkage of the part along the printing direction during the EB-PBF process and cooling had a consistent trend, which was not affected by overall part length, shape, wall thickness and printing orientation of the part. The nonlinearity of shrinkage led to more geometric errors in the part at the lower half from the base plate than in the upper half along the part height. The results explained why linear scaling factors generally worked well for small-size components when height was less than 60 mm, as shown in Figure 4(b), but not suitable for large-scale components and assemblies with part lengths over 300 mm due to the distortion nonlinearity. The findings indicated the shrinkage of the EB-PBF part was mainly influenced by thermal history in the process and temperature distribution in the build chamber.

Figure 5 presents the averaged shrinkage rate of each interval between measuring marks. Along the X or Y direction, the shrinkage of each length interval of 10 mm was less than 0.7 % on average. The averaged absolute shrinkage values at each interval were 25.4 μm in X and 69.5 μm in Y, which was close to the tolerance of measurement accuracy (0.09 mm) considering the influence of surface roughness [31]. Therefore, the deviation between each interval is not statistically significant, indicating a uniform shrinking behaviour of the component along X and Y directions. Figure 5(b) plots the shrinkage rate at every interval of 25 mm between pilot holes of both long bracket samples. The results showed larger deviations between the first three intervals than the remainders. With a decreasing trend from the maximum shrinkage rate of 1.22 % at the first interval, a stable shrinkage rate of 0.42 % can be found from interval 5 to 11, which was smaller than the averaged rate along the X direction. The first three intervals from the base plate represented the zone with the highest shrinkage rate. The observed nonlinear distortion rules affect the design for EB-PBF and its compensation strategies, indicating the results have engineering significance. In the case of bracket printing, the distribution of dimensional deviations were different because of opposite printing orientations. For instance, the topological deviations were different because of opposite printing orientations. For instance, the topological optimised (TO) area in the bracket deformed approximately 0.6 mm more in Orientation 1 than the Orientation 2. Therefore, printing with Orientation 2 led to better dimensional stability for the critical load-bearing features, highlighted in the dash-line box. It can be advisable to position the critical features at a height exceeding 125 mm within the chamber to minimise thermal shrinkage. The findings must be considered in the nonlinear compensation of the deformation. Moreover, the interactions between X and Y directions were visualised in Figure 5(c). A planar shrinkage percentage $\psi_{(i,\ j)}$ was evaluated at the height of measuring marks with an equation,

$$\psi_{(i,j)} = \frac{\sqrt{\varphi_i^2 + \varphi_j^2}}{\sqrt{10^2 + 10^2}}, \tag{3}$$

where φ_i and φ_j are the constitutive shrinkage magnitude at the i^{th} and j^{th} intervals along x and y directions in mm, respectively. The contour mapping assumes zero deformation at the centre (original point) of the XY plane, showing a gradually increasing shrinkage rate from centre towards the surrounding region. In addition, the resultant shrinkage rate at various locations in 3D space can be further estimated from the constitutive findings at every unit voxel of 10 mm × 10 mm × 25 mm. The resultant shrinkage rate of one unit voxel $\psi_{(i,\ j,\ k)}$ can be calculated with the equation,

$$\psi_{(i,j,k)} = \frac{\sqrt{\varphi_i^2 + \varphi_j^2 + \varphi_k^2}}{\sqrt{10^2 + 10^2 + 25^2}}, \tag{4}$$

where φ_k is the constitutive shrinkage magnitude at the k^{th} interval along the z direction in mm. Global mapping of the resultant shrinkage rate is shown in Figure 5(d). The contour indicated that the thermal deformation was more obvious in certain areas of the chamber with a height less than approximately 125 mm from the base plate. In this area, shrinkage along the Z direction was dominating, as illustrated in Figure 5(d). A higher shrinkage rate was expected to be obtained when the component was positioned closer to the base plate. The height effect was also observed in Figure 5(d'') with contour maps at X-Y cross-sections with different heights. There was no significant diversity in the resultant shrinkage rate when the build height was higher than approximately 200 mm because the effect of the shrinkage component along the Z direction was reduced, and planar shrinkage played a dominant role.

3.2. Thermal-mechanical simulation results

We developed a coupled thermal-mechanical model to simulate the EB-PBF printing and cooling process to further investigate the nonlinear shrinkage along the part height direction. Figure 6(a) presents the computed shrinkage of the bracket component and its correlation with measured data. Overall, the simulation results captured the magnitude of the deformation with a nonlinear accumulation trend. However, the nonlinear effect was underestimated, likely due to simulation simplifications. The Mean Absolute Percentage Error (MAPE) was calculated as 13.93 %, 18.97 % and 17.40 % for the free faces, respectively, indicating a reasonable model accuracy [43]. Figure 6(b) plots the contour of the displacement, showing that the shrinkage rate along Z direction was also affected by the part width. The findings agreed well with a slight deviation of measured data from the three bracket faces (Figure 4(c) and (d). The contour reflected that shrinkage near the edge was smaller than in the centre area because heat dissipated by loose powers was lower than that by solidified materials. The edge effect was not considered in the proposed compensation approach since the part width was smaller than 60 mm and less significant compared to the height in this bracket demonstrator.

Moreover, simulation results indicated the nonlinearity was progressively formed from the printing stage. In the EB-PBF process, when each new layer was additively manufactured, previous layers started to cool and shrink. The temperature history experimentally obtained at the base plate is shown in Figure 7(a). It was preheated to approximately 730 °C at the start of the print and nonlinearly cooled down to 622 °C while the part was continuously built. Computed temperature histories at the height of each hole were also plotted, with similar decrement patterns. Once the printing was completed, the component continued to cool down at a higher cooling rate until room temperature. At the beginning of this stage, the temperature distribution was nonlinear,

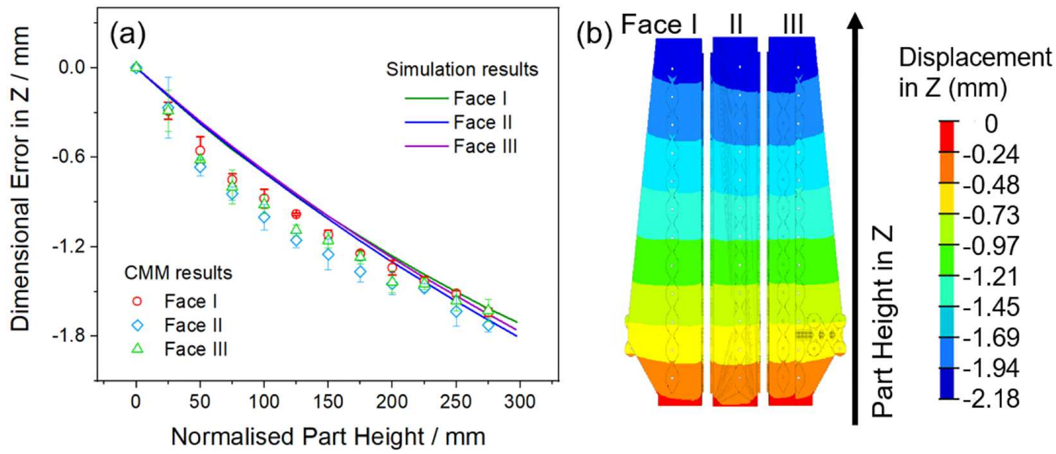

Figure 6. (a) Computed shrinkage of the demonstrator compared with CMM observations and (b) shrinkage contours on three faces.

although the hole interval was identical. Accordingly, dimensional error and thermal stress distributions at each hole interval were monitored during the process simulation, and Figure 7(b) and (c) show results obtained at the end of the printing stage and at the end of the cooling stage, respectively. When the printing was completed, the first interval exhibited the largest degree of shrinkage, attributed to the highest thermal stress and

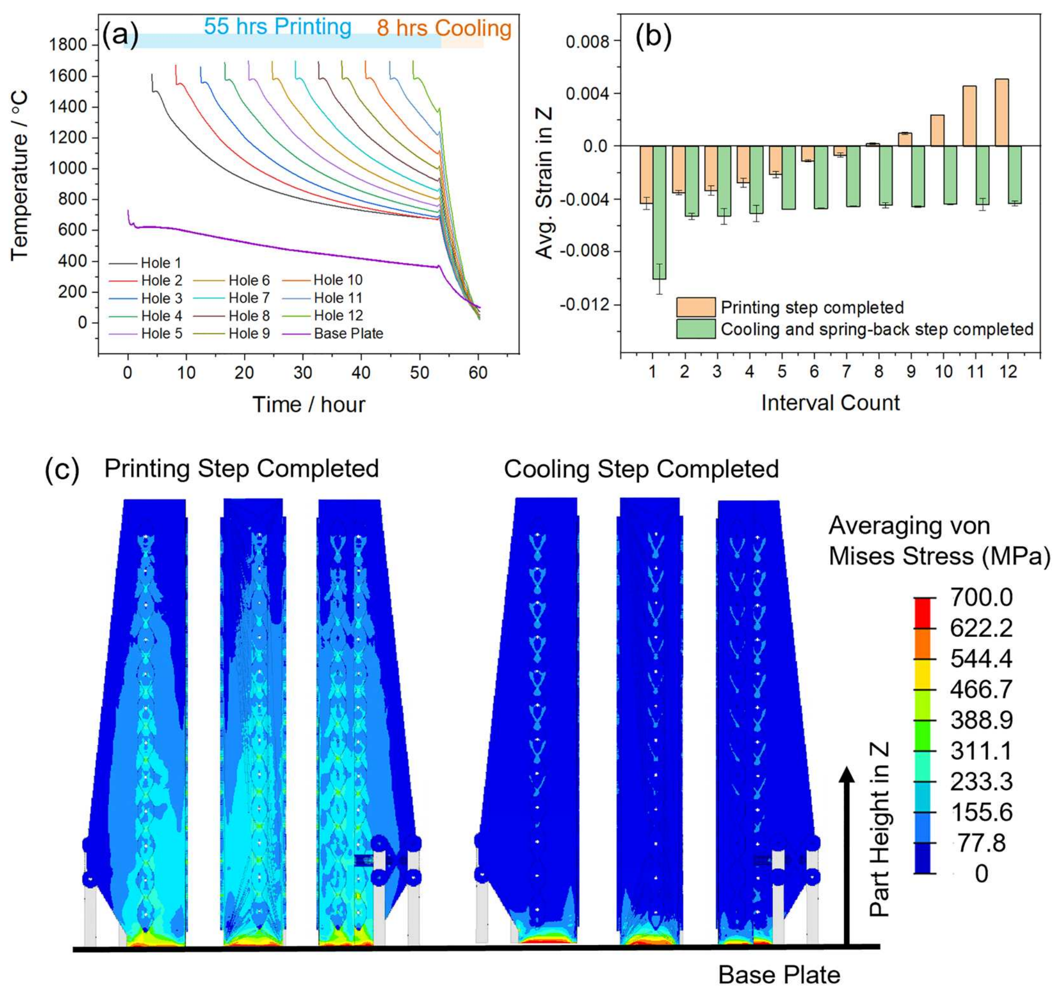

Figure 7. (a) Computed temperature history at the height of each pilot hole with measured temperature history at base plate, (b) computed averaging strain of each interval and (c) thermal stress contour before and after cooling stage.

a longer duration of cooling at the lower region. The deformation of the lower section was affected by constraints imposed by the supports and base plate. The intervals 9–12 were expanded as the temperature of those areas still exceeded 1000 °C and the thermal stress was therefore relatively lower. At the cooling stage, the dimensional error was attributed to both temperature change and thermal stress relief. At the end of cooling, residual stress was at a very low level, except for the concentration found at the constrained region between the component and base plate. Such a high residual stress led to spring-back when the component was removed from the base plate [44].

The compensation for thermal shrinkage of the bracket shape can be conducted based on the presented simulation results. Every node was morphed towards the opposite direction from the computed displacement components. The compensated shape was then used for process modelling with the same parameters. Furthermore, the proposed nonlinear compensation method was applied to the bracket component derived from the interpolation of distortion measurement along the Z direction. To compare with the above two methods, a uniform single scaling factor of 1.0061, calculated from the total shrinkage of overall part height, was also applied. After re-printing the compensated components, the dimensional errors were measured again with CMM. Figure 8 compares the results of dimensional error along the Z direction from three compensation approaches. It was found that the linear scaling approach resulted in a nonlinear geometric error, giving a maximum deviation of up to 0.34 mm from a build height of up to 300 mm, although overall part shrinkage was minimised around zero. This fact indicated that nonlinear thermal shrinkage of EB-PBF parts will not maintain a fully reversible deformation compared to that from linear shrinkage. For the same reason, as results of process modelling for compensated shapes, the numerical solution of dimensional error was non-zero after node-morphing compensation, with a maximum deviation of up to 0.22 mm amongst the computed positions of the measuring marks. The practical outcome of simulation-based compensation strongly depends on model validation because the MAPE between simulation results and experiments may further decline the effectiveness. In contrast, the proposed nonlinear compensation showed its advantage as the maximum error along the z-direction was successfully reduced to an average of 0.16 mm, smaller than the result from the scaling method. Most of the measured data fall within the zero-error threshold band, attributed to the 0.09 mm measurement error of the CMM. More importantly, the nonlinear compensation approach managed to minimise the dimensional error at every interval along the component, fulfilling the tolerance requirement for part assembly.

4. Discussion

This study systematically investigated the orthogonally anisotropic thermal shrinkage behaviour of Ti-6Al-4V parts fabricated by EB-PBF and developed and compared 3D compensation strategies to minimise dimensional errors in large-scale industrial components. The findings reveal that shrinkage rates in the X and Y directions remain relatively linear irrespective of build flatform location, while the Z direction exhibits significant nonlinear shrinkage as a function of build height.

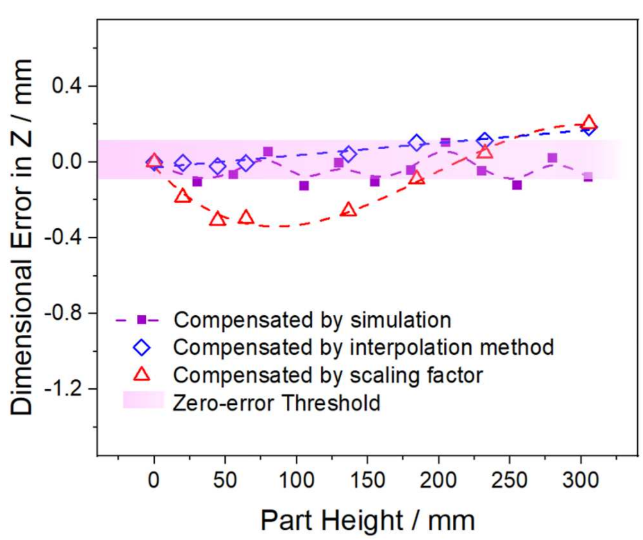

Figure 8. Comparison of dimensional errors along part height between linear, simulation and nonlinear compensation methods.

This discrepancy in shrinkage behaviour is primarily attributed to the complex temperature gradients, the accumulation and release of thermal stresses, and the thermal expansion and contraction behaviour along the Z axis during the EB-PBF process. In the XY plane, although it is theoretically assumed that the temperature field is uniformly distributed, in practice, due to the design of the EB-PBF build chamber, boundary effects, and differences in thermal conduction between the front-back and left-right positions, the temperature gradients in the X and Y directions are not uniform [45]. This uneven thermal conduction leads to asymmetric shrinkage in the XY plane. While the variation in shrinkage rates across the XY plane is relatively small, the underlying thermal asymmetry is a critical factor affecting dimensional accuracy. Our results were obtained from an Arcam A2X machine and systematically validated. The validation process involved a set of geometries with dimensions ranging from 30 to 345 mm, covering a diverse range of design configurations. We believe that our conclusions can be extended to the full build envelope of the A2X machine, which measures 200 × 200 × 380 mm^3. It is suggested that different machines, such as those with larger build chambers (e.g. Arcam EBM Q20plus [46]) or circular build platforms (e.g. Spectra H [47]), may exhibit more uniform shrinkage behaviour in the XY direction. The nonlinear shrinkage behaviour in the Z direction is particularly pronounced in larger components, especially those with a high aspect ratio. This phenomenon is closely related to the gradual accumulation and release of thermal stress during cooling. Our simulations indicate that this nonlinear shrinkage develops progressively throughout the printing process. In EB-PBF, as each new layer of material is added, the previously deposited layers begin to cool and shrink. Experimental data on the substrate temperature history show that the substrate is preheated to approximately 730 °C at the start of printing and nonlinearly cools to 622 °C as the part is built layer by layer (Figure 7(a)). A similar cooling pattern is observed at various measured heights. After printing is completed, the part cools rapidly to room temperature, with a nonlinear temperature distribution throughout this process, even though the spacing between the measured points is constant. The nonlinear shrinkage in the Z direction is primarily driven by the accumulation of thermal stresses, the non-uniform temperature distribution, and the temperature-dependent nonlinear behaviour of the Ti-6Al-4V material.

While traditional linear compensation methods may be effective for smaller parts such as acetabular cups [48], impellers [49], and compliant mechanisms [50], they fail to meet the dimensional accuracy requirements of complex structures, particularly large components with high aspect ratios, such as turbine blades or topology-optimised lightweight designs [9]. In topology-optimised structures, variations in dimensional accuracy can result in uneven stress distributions across different regions [51]. Significant shrinkage in certain areas may alter the stress distribution, compromising the overall structural performance and preventing the design from achieving its intended optimal performance. The 3D compensation method proposed in this study effectively reduces geometric errors (Figure 8). By accounting for nonlinear shrinkage behaviour along printing direction and orthotropically discrepant shrinkage along X and Y, this method is better suited for the printing and optimisation of complex industrial parts. Nevertheless, it is challenging to mitigate distortion of overhanging structures through compensation. Instead, an appropriate design of support structures is critical.

Ideally, high-fidelity process simulations could be a precise way to predict the thermal deformation of AM components and effectively compensate for the deformation in the design stage. However, two major challenges affect the accuracy and efficiency of the numerical methods. One challenge is associated with length scales. Across multiple length scales, the constitutive laws considered in modelling diverge. For instance, heat source, powder stacking, and phase transformation are commonly discussed in micro-scale models. Most simulation studies on the macro scale are conducted with simple shapes and voxel meshes with maximum dimensions of less than 120 mm for adopting detailed constitutive physical laws and better feasibility of experimental validation. Furthermore, voxel meshes cause fidelity loss when re-creating printing files. The other challenge is the lack of commercial software packages developed for the EB-PBF process and validated through industrial utilisation. To the authors' knowledge, the majority algorithms were developed for the L-PBF process, including Print3D. The process uncertainty, in addtion to inaccurate boundary conditions of EB-PBF AM, always impedes model validations. With the above gaps, compensation based on simulation results may not lead to an accurate part dimension after printing. Therefore, cycles of measurement and adjustment are still necessary. This study managed to capture the nonlinear deformation we observed in experiments with commercially available thermal-mechanical models, obtaining the averaged MAPE indicator of approximately 16.8 %. Based on current findings, some key learning points can be discussed regarding the trade-off between model effectiveness and an acceptable computational cost when defining process boundary conditions and material property input.

When applying various material properties from the literature, the simulation results showed significant variations. In parameter studies, we compared computing results with experimental observations. As illustrated in Figure 9, through parameter studies, we identified the critical material input, such as Young's modulus, yield stress and emissivity that would significantly affect the prediction of shrinkage magnitudes and respective degrees of nonlinearity. This is attributed to the temperature-dependent nature of these property values. Properties of the material at room temperature were not applicable due to elevated preheating temperature of the base plate in the EB-PBF process. However, a single value of material input saves computational time. When testing main temperature-dependent properties with a single variable method, it was further implied that the effects of density, specific heat, conductivity and Poissons' ratio on deformation nonlinearity were not significant compared with the ones listed in Figure 9. Similarly, the scanning velocity and the power of the heat source have also been found to be the main processing factors that affect the shrinkage behaviour. The findings from simulation studies not only helped validation of the model with a decent computational cost, but also indicated significant factors that corelate to shrinkage behaviour. In future work, more detailed models of heat source and scanning should be developed to improve EB-PBF process simulation results. Moreover, current limitations can also be found in simplifications of thermal boundary conditions. Experimental observations indicated temperature distribution inside the chamber contributed to the interaction between the powder bed and components, leading to a nonlinear deformation.

The geometrical compensation for nonlinear deformation is another topic that needs further investigation. Different from linear deformation that can be compensated entirely, there is no reversible mapping for nonlinear deformation. A node at a compensated position follows a new deformation mapping, leading to a remaining dimensional error. Therefore, it is crucial to unveil nonlinear deformation rules, making the mapping predictable. Current results indicated that the rules are independent of the overall shape, height and printing orientations of the component under a given

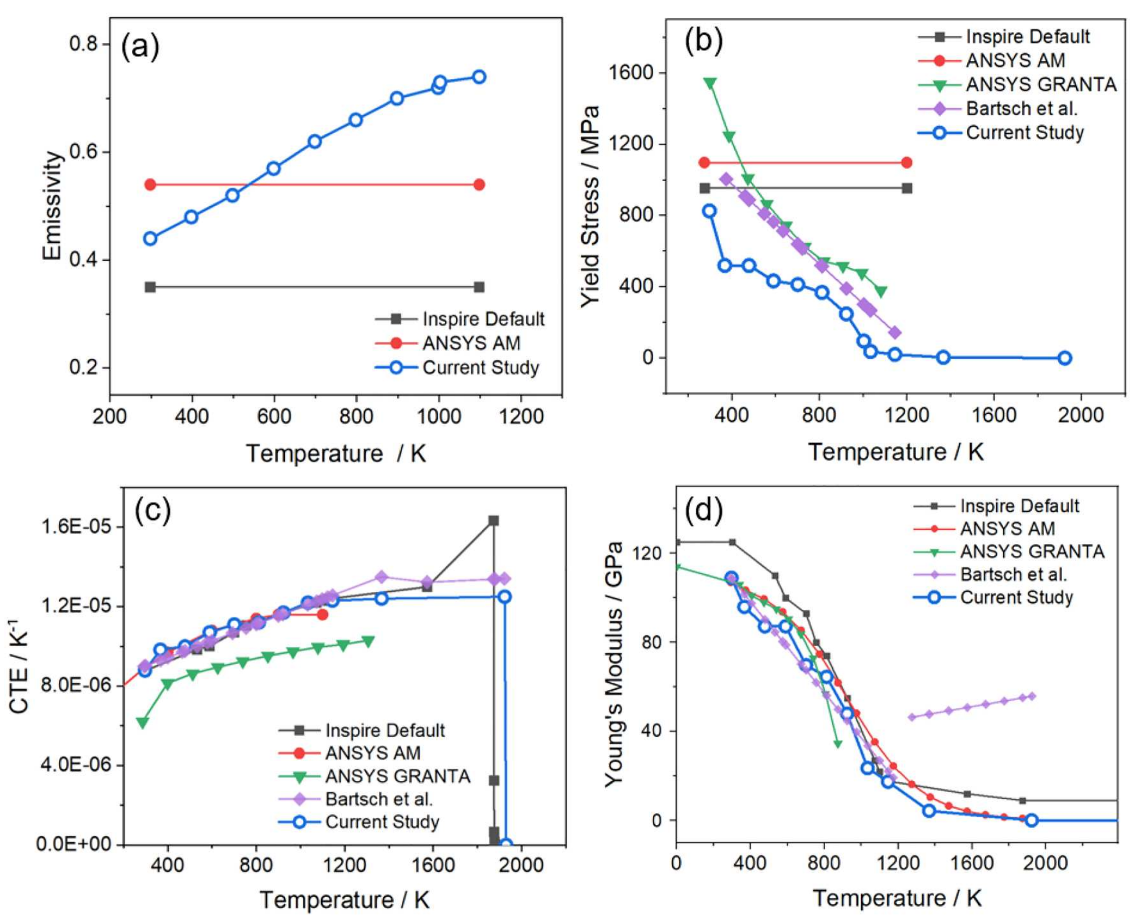

Figure 9. Critical temperature-dependent material properties used for simulation in this study and comparison with varying sources and software database [9,34,37–41]: (a) Emissivity, (b) yield stress, (c) coefficient of thermal expansion and (d) Young's modulus.

material type and process parameter set. With a clear nonlinear trend of deformation, the compensation methods proposed in this study minimised the remaining dimensional error to an acceptable level for large-scale industrial components. However, more work can be done to consider a mathematical description of the deformation as functions of key material input and process parameters, leveraging current findings to a wide application for EB-PBF in the industry.

In the EB-PBF process, in addition to Ti-6Al-4V, materials such as IN718 [40,52,53] and titanium aluminide (including Ti-48Al-2Cr-2Nb [54], Ti-45Al-4Nb [55], etc.) are also widely used in industrial manufacturing. Their material properties, including coefficient of thermal expansion, Young's modulus, yield strength, and emissivity, differ significantly from Ti-6Al-4V, which is expected to have profound effects on shrinkage behaviour in various directions. Firstly, the powder-bed temperatures for IN718 and titanium aluminide are relatively higher, typically ranging from 950 °C to 1150 °C [56,57], whereas Ti-6Al-4V is printed at a lower temperature. This temperature difference leads to variations in how thermal stress is accumulated and released. For instance, higher printing temperatures induce steeper thermal gradients, potentially resulting in more pronounced shrinkage [58]. Given that IN718 and titanium aluminide exhibit higher yield strength and stronger resistance to high-temperature creep, they tend to retain greater residual stress during cooling, posing more complex challenges for dimensional compensation in the 3D directions. Moreover, the material-substrate interface also affects shrinkage behaviour. For example, in Ti-6Al-4V printing, a steel start plate is typically used as the substrate, where intermetallic compound layers can form at the interface [59]. Due to the mismatch in thermal expansion coefficients, this interface is prone to delamination during cooling, thereby releasing stress. However, when printing IN718 with the same steel substrate, the transition layer formed at the interface is more stable [60] and does not effectively release the stress within the bottom region that easily, which may result in greater deformation near the base [58]. This suggests that the shrinkage behaviour in the bottom region of IN718 parts requires particular attention and compensation. Therefore, while Ti-6Al-4V, IN718, and titanium aluminides share certain characteristics in the EB-PBF process, their differing material properties and printing conditions necessitate tailored shrinkage compensation strategies alongside detailed experimental validation. For IN718 and titanium aluminides, the higher printing temperatures and distinct mechanical behaviours result in a more pronounced nonlinear shrinkage in the Z direction, while stress release and deformation in the bottom regions require more precise control. In addition to these high-temperature materials, other alloys, such as pure titanium [61], beta titanium alloys [62,63], aluminium alloys [64], pure copper [65], copper alloys [66], and high-entropy alloys [67–71], may require printing temperatures similar to or lower than that of Ti-6Al-4V. Each of these materials has unique thermal and mechanical properties, demanding distinct approaches to printing and shrinkage compensation. Besides the material chemical composition, another potential consideration is the powder characteristics, as they have been shown to influence the melt pool shape and laser absorption rate [69]. However, we found that powder characteristics have only a minimal impact on electron beam absorption, resulting in relatively small changes to the overall temperature distribution [56,66]. Therefore, we believe that powder characteristics do not have a noticeable effect on the final parts' dimensional accuracy, given that the critical factor for dimensional accuracy remains the temperature distribution within the build envelope. With assumptions and methodologies validated in this study, the 3D compensation method can be leveraged to more EB-PFB material systems.

5. Integration of compensation methods into the AM design workflow towards an end-to-end solution: application through a case study

Based on the anisotropic shrinkage rules of the EB-PBF process concluded for Ti-6Al-4V in this study, we developed a 3D nonlinear compensation method for large-scale components. The compensation method can be integrated with design workflow for AM and close the loop of the EB-PBF process to provide an end-to-end solution that avoids printing trials and iterations of error measurement. Figure 10 illustrates a comprehensive case study to demonstrate the application of re-designing a component for the EB-PBF process and manufacturing it with minimal dimensional errors. The component was inspired by a generative design case for a satellite supporting bracket [72,73]. The original design of the bracket was a metal flange structure involving a number of bolts or an extensive welding process for assembly, as per Figure 10(a). The bracket is used as a connector to mount various parts with the main body of a satellite, therefore requiring dimensional accuracy for mounting positions. Instead of using sheet metal, the design space was defined as a bulk with symmetrical constraints and various loading cases. An overhang angle constraint of 60° was also included as featured in the design to the EB-PBF process (Figure 10(b)). After

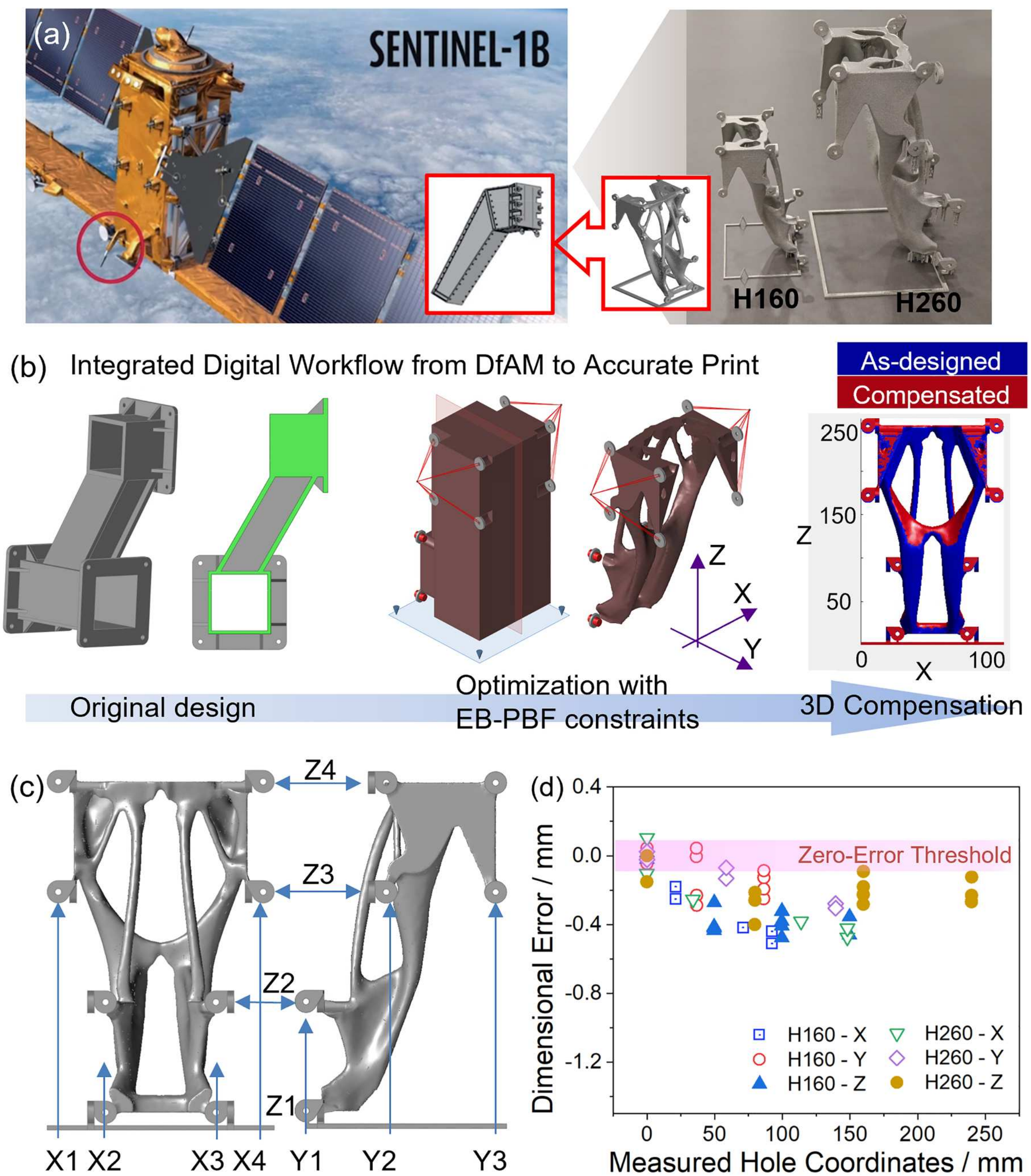

Figure 10. An integrated digital workflow to (a) re-design a satellite component for EB-PBF processes as a case study. The workflow starts from (b) analysis of the original shape, defining design space, topology optimisation for preliminary design, shape regeneration and applying nonlinear compensation to obtain new designs with different heights (160 and 260 mm) for prototyping. (c) The compensated shapes were ready-to-print with multiple measuring marks. (d) Dimensional errors were evaluated with CMM.

topology optimisation and structural reanalysis, a new shape achieving around 20.3 % weight reduction was obtained. The global size of the component was approximately 164 mm × 154 mm × 260 mm. To compensate for the shrinkage, the same 3D compensation method developed in this study, based on measurement results from the beam samples and the long bracket, was applied to each node of the STL file. Herein, the previously determined scaling factors for the X and Y directions and interpolation equations in the Z direction were leveraged to describe the predicted dimensional error in the current case. By adopting such a method, it is not necessary to repeat cycles of 'print-measure-compensate' for different components under the same fabrication conditions.

In this case study, pilot holes were designed as measuring marks for dimensional check after printing, as illustrated in Figure 10(c). The designed component was prepared in two heights, 160 and 260 mm, respectively, denoted H160 and H260. Two shapes were compensated and prototyped. After printing and removing from the base plates, the coordinates of the holes were measured and compared with designed values, and the dimensional differences were presented in Figure 10(d). Results from both H160 and H260 components showed good dimensional accuracy with the largest errors were approximately 0.44 and 0.47 mm, respectively. Based on finding of the beam and bracket shapes we measured, the max dimension error of H160 and H260 can be estimated as around 1.2 and 1.7 mm respectively. Considering the influence of measurement accuracy, the obtained errors were very minor, comparing to the zero-error threshold. It was noted that dimensional error in the Z direction was generally less than those in the X direction, showing the benefit of using the integrated design to nonlinear compensation approach for preparing different shapes for the EB-PBF process. Although the method was still applied to only the same Ti-6Al-4V material and the same process parameters in the case study, it has the potential to be extended to more material powders and processes. To achieve this, further experimental work is needed to calibrate the nonlinear shrinkage trends of various materials. Correlation between material properties and the shrinkage rules can be built with the assistance of validated process simulations and data-driven methods. Beyond EB-PBF, the approach proposed in this study can be also leveraged to other AM processes to investigate the applicability and feasibility of applying the 3D compensation method.

6. Conclusions

This study systematically investigated orthotropic thermal shrinkage of Ti-6Al-4 V parts fabricated by EB-PBF processes and developed a 3D compensation method to minimise dimensional errors of large-scale industry components. A series of L-shaped beams (length up to 130 mm), rectangular vertical beams and thin-wall bracket components (height up to 330 mm) were designed with an array of measuring marks to capture the basic thermal deformation along three global coordinate directions. Specifically, the shrinkage magnitudes and accumulation trends were analysed with CMM by measuring the coordinates of marks with identical intervals. It was found that the overall shrinkage rate was stable at approximately 0.69% along the X direction and 0.26% along the Y direction, indicating a uniform shrinkage accumulation in these directions. However, a nonlinear shrinkage was observed along the Z direction. Here, a significant shrinkage rate of up to 1.29% was found at the lower 125 mm from the base plate, while it was progressively reduced to 0.6 % by averaging at the higher end of the component. Along the Z direction, the total shrinkage averaged 1.81 ± 0.01 mm over a 300 mm part height, and this was consistently validated across different shapes and printing orientations. Simulation results from a coupled thermal-mechanical model of the EB-PBF process indicated that the experimentally determined nonlinearity arose from (i) thermal stress accumulation and relief in the EB-PBF process, (ii) nonuniform temperature distributions at different layers of as-printed parts, and (iii) temperature-dependent material nonlinearity of Ti-6Al-4V. Furthermore, a 3D compensation method was successfully developed to increase the printing accuracy of the EB-PBF process. Compared with compensation by applying a scaling factor and reverse-morphing of simulation results, the proposed method based on nonlinear shrinkage rules not only compensated the total shrinkage but also reduced the dimensional error of every interval, with a maximum error of 0.16 mm. This method was integrated into a digital workflow and applied in a case study where a satellite component was re-designed and topologically optimised for EB-PBF. We have hence demonstrated that the current approach optimises the end-to-end solution for EB-PBF Ti-6Al-4V by minimising geometric errors, reducing post-processing, and shortening trial cycles, ultimately lowering costs.

Acknowledgement

This research was supported by the Agency for Science, Technology and Research (A*STAR) of Singapore under Career Development Fund (C210112043) and the Manufacturing, Trade and Connectivity (MTC) Programmatic Grant Advanced models for Additive Manufacturing (AM2) (M22L2b0111). The authors would like to express their sincere gratitude to Ms. Yuchan Liu for her valuable contributions to the investigation and her guidance on CMM measurements.

Disclosure statement

No potential conflict of interest was reported by the author(s).

Funding

This work was supported by Agency for Science, Technology and Research [grant number: C210112043] and the Manufacturing Trade and Connectivity Programmatic Fund [grant number: M22L2b0111].

Author contribution

Chen Wang: Conceptualisation, Methodology, Formal analysis, Investigation, Data curation, Simulation work, Topology Optimisation, Writing – original draft, Writing – review & editing, Visualisation, Project administration, Funding acquisition. **Chen-Nan Sun**: Discussion, Writing – review & editing, Experiment guide. **Lei Zhang**: Compensation method development, Investigation. **Stefanie Feih**: Conceptualisation, Methodology. **Pan Wang**: Methodology, Discussion, Formal analysis, Visualisation, Writing – original draft, Writing – review & editing, Project administration, Data interpolation, Funding acquisition.

Data availability statement

The authors confirm that the data supporting the findings of this study are available within the article.

ORCID

Chen Wang http://orcid.org/0000-0002-6899-035X
Chen-Nan Sun http://orcid.org/0000-0002-9304-0495
Lei Zhang http://orcid.org/0000-0002-6553-4412
Stefanie Feih http://orcid.org/0000-0003-2442-3326
Pan Wang http://orcid.org/0000-0002-2079-9580

References

[1] Technavio. Metal Additive Manufacturing Market by Type, Application, and Geography – Forecast and Analysis 2023-2027. Published: May; 2023.

[2] Zhu ZG, Hu ZH, Seet HL, et al. Recent progress on the additive manufacturing of aluminum alloys and aluminum matrix composites: microstructure, properties, and applications. Int J Mach Tools Manuf. 2023;190:104047. doi:10.1016/j.ijmachtools.2023.104047

[3] Sarkar D, Kapil A, Sharma A. Advances in computational modeling for laser powder bed fusion additive manufacturing: A comprehensive review of finite element techniques and strategies. Addit Manuf. 2024;85:104157.

[4] Bandyopadhyay A, Traxel KD. Invited review article: metal-additive manufacturing—modeling strategies for application-optimized designs. Addit Manuf. 2018;22:758–774.

[5] Yaghi A, Ayvar-Soberanis S, Moturu S, et al. Design against distortion for additive manufacturing. Addit Manuf. 2019;27:224–235. doi:10.1016/j.addma.2019.03.010

[6] He B, Bi C, Li X, et al. Residual stresses and deformations of laser additive manufactured metal parts: a review. Int J Mater Form. 2023;16:7. doi:10.1007/s12289-022-01729-w

[7] Mercelis P, Kruth JP. Residual stresses in selective laser sintering and selective laser melting. Rapid Prototyp J. 2006;12(5):254–265. doi:10.1108/13552540610707013

[8] Bartlett JL, Li X. An overview of residual stresses in metal powder bed fusion. Addit Manuf. 2019;27:131–149. doi:10.1016/j.addma.2019.02.020

[9] Wang P, Song J, Nai MLS, et al. Experimental analysis of additively manufactured component and design guidelines for lightweight structures: A case study using electron beam melting. Addit Manuf. 2020;33:101088. doi:10.1016/j.addma.2020.101088

[10] Afazov S, Okioga A, Holloway A, et al. A methodology for precision additive manufacturing through compensation. Precis Eng. 2017;50:269–274. doi:10.1016/j.precisioneng.2017.05.014

[11] Peng X, Huang Q, Zhang G, et al. Compensating the anisotropic mechanical properties of electron beam melting-based gyroid scaffolds using structural design. Int J Mechan Sci. 2022;226:107442. doi:10.1016/j.ijmecsci.2022.107442

[12] Chen C, Xiao Z, Zhu H, et al. Deformation and control method of thin-walled part during laser powder bed fusion of Ti–6Al–4V alloy. Int J Adv Manuf Technol. 2020;110(11–12):3467–3478. doi:10.1007/s00170-020-06104-0

[13] Ghaoui S, Ledoux Y, Vignat F, et al. Analysis of geometrical defects in overhang fabrications in electron beam melting based on thermomechanical simulations and experimental validations. Addit Manuf. 2020;36:101557. doi:10.1016/j.addma.2020.101557

[14] Ledoux Y, Ghaoui S, Vo TH, et al. Geometrical defect analysis of overhang geometry produced by electron beam melting: experimental and statistical investigations. Int J Adv Manuf Technol. 2022;122(3–4):2059–2075. doi:10.1007/s00170-022-10040-6

[15] Cheng B, Chou K. Geometric consideration of support structures in part overhang fabrications by electron beam additive manufacturing. CAD Comput Aided Des. 2015;69:102–111. doi:10.1016/j.cad.2015.06.007

[16] Zafar MQ, Wu CC, Zhao H, et al. Finite element framework for electron beam melting process simulation. Int J Adv Manuf Technol. 2020;109(7–8):2095–2112. doi:10.1007/s00170-020-05707-x

[17] Dong W, Jimenez XA, To AC. Temperature-dependent modified inherent strain method for predicting residual stress and distortion of Ti6Al4V walls manufactured by wire-arc directed energy deposition. Addit Manuf. 2023;62:103386. doi:10.1016/j.addma.2022.103386

[18] Franchitti S, Borrelli R, Pirozzi C, et al. Investigation on electron beam melting: dimensional accuracy and process repeatability. Vacuum. 2018;157(November):340–348. doi:10.1016/j.vacuum.2018.09.007

[19] Zhao X, Wei Y, Mansour R, et al. Effect of scanning strategy on thermal stresses and strains during electron beam melting of inconel 625: experiment and simulation. Materials (Basel). 2023;16(1):443. doi:10.3390/ma16010443

[20] Yin Q, Wei H, Chen R, et al. Interdependent evolution of deformation, fracture and recovering deposition during laser powder bed fusion. Addit Manuf. 2023;72(April):103610. doi:10.1016/j.addma.2023.103610

[21] Xie D, Lv F, Yang Y, et al. A review on distortion and residual stress in additive manufacturing. Chin J Mechan Eng Addit Manuf Front. 2022;1(3):100039. doi:10.1016/j.cjmeam.2022.100039

[22] Juechter V, Scharowsky T, Singer R, et al. Processing window and evaporation phenomena for Ti–6Al–4V produced by selective electron beam melting. Acta Mater. 2014;76:252–258. doi:10.1016/j.actamat.2014.05.037

[23] Khrapov D, Kozadayeva M, Koptyug A, et al. Geometrical features and mechanical properties of the sheet-based

gyroid scaffolds with functionally graded porosity manufactured by electron beam melting. Mater Today Commun. 2023;35:106410. doi:10.1016/j.mtcomm.2023.106410

[24] Afazov S, Semerdzhieva E, Scrimieri D, et al. An improved distortion compensation approach for additive manufacturing using optically scanned data. Virtual Phys Prototyp. 2021;16(1):1–13. doi:10.1080/17452759.2021.1881702

[25] Hong R, Zhang L, Lifton J, et al. Artificial neural network-based geometry compensation to improve the printing accuracy of selective laser melting fabricated sub-millimetre overhang trusses. Addit Manuf. 2021;37:101594.

[26] Smith CJ, Derguti F, Hernandez Nava E, et al. Dimensional accuracy of electron beam melting (EBM) additive manufacture with regard to weight optimized truss structures. J Mater Process Technol. 2016;229:128–138. doi:10.1016/j.jmatprotec.2015.08.028

[27] Zhang Z, Xie D, Lv F, et al. Intelligent geometry compensation for additive manufactured oral maxillary stent by genetic algorithm and backpropagation network. Comput Biol Med. 2023;157:106716. doi:10.1016/j.compbiomed.2023.106716

[28] Dalpadulo E, Pini F, Leali F. Powder bed fusion integrated product and process design for additive manufacturing: a systematic approach driven by simulation. Int J Adv Manuf Technol. 2024;130:5425–5440. doi:10.1007/s00170-024-13042-8

[29] Soundararajan B, Sofia D, Barletta D, et al. Review on modeling techniques for powder bed fusion processes based on physical principles. Addit Manuf. 2021;47:102336. doi:10.1016/j.addma.2021.102336

[30] Wang P, Li X, Luo S, et al. Additively manufactured heterogeneously porous metallic bone with biostructural functions and bone-like mechanical properties. J Mater Sci Technol. 2021;62:173–179. doi:10.1016/j.jmst.2020.05.056

[31] Wang C, Sin WJ, Liu YC, et al. Distortion discrepancy of large-scale components in electron beam melting processes. Mater Today: Proc. 2022;70:61–65. doi:10.1016/j.matpr.2022.08.529

[32] Wang P, Sin W, Nai M, et al. Effects of processing parameters on surface roughness of additive manufactured Ti-6Al-4V via electron beam melting. Materials (Basel). 2017;10:1121. doi:10.3390/ma10101121

[33] Altair, Altair Inspire User Guide, 2022. https://2022.help.altair.com/2022/inspire/en_us/index.htm

[34] Denlinger ER. Residual stress and distortion modeling of electron beam direct manufacturing Ti-6Al-4 V. 1st ed. In: *Thermo-Mechanical modeling of additive manufacturing*. Butterworth-Heinemann; 2018. p. 153-166. doi:10.1016/B978-0-12-811820-7.00011-2

[35] Bayraktar C, Demir E. A thermomechanical finite element model and its comparison to inherent strain method for powder-bed fusion process. Addit Manuf. 2022;54:102708. doi:10.1016/j.addma.2022.102708

[36] Gouge M, Michaleris P, Denlinger E, Irwin J. The finite element method for the thermo-mechanical modeling of additive manufacturing processes. 1st ed. In: *Thermo-Mechanical modeling of additive manufacturing butter-worth-heinemann*. Butterworth Heinemann; 2018; p. 19–38. doi:10.1016/B978-0-12-811820-7.00003-3

[37] ANSYS, ANSYS Additive Users Guide Print and Science 2021R1. 2021.

[38] ANSYS, Ansys Granta Selector 2022 User Manual and Getting Started Guide. 2022.

[39] Bartsch K, Herzog D, Bossen B, et al. Material modeling of Ti–6Al–4V alloy processed by laser powder bed fusion for application in macro-scale process simulation. Mater Sci Eng A. 2021;814:141237. doi:10.1016/j.msea.2021.141237

[40] Wang P, Ng FL, Nai MLS, et al. Towards the mechanism of in situ welding during electron beam powder bed fusion process. Mater Sci Eng 2022;858:144170. doi:10.1016/j.msea.2022.144170

[41] Parry L, Ashcroft IA, Wildman RD. Understanding the effect of laser scan strategy on residual stress in selective laser melting through thermo-mechanical simulation. Addit Manuf. 2016;12:1–15.

[42] Guo J, Goh MH, Wang P, et al. Investigation on surface integrity of electron beam melted Ti-6Al-4 V by precision grinding and electropolishing. Aeronaut. 2021;34(12):28–38. doi:10.1016/j.cja.2020.08.014

[43] Ness KL, Paul A, Sun L, et al. Towards a generic physics-based machine learning model for geometry invariant thermal history prediction in additive manufacturing. J Mater Process Technol. 2022;302:117472. doi:10.1016/j.jmatprotec.2021.117472

[44] Li L, Anand S. Fast additive manufacturing distortion prediction using backward interpolation. Addit Manuf. 2021;41:101955. doi:10.1016/j.addma.2021.101955

[45] Landau E, Tiferet E, Ganor YI, et al. Thermal characterization of the build chamber in electron beam melting. Addit Manuf. 2022;36:101535.

[46] Kermavnar T, Shannon A, O'Sullivan LW. The application of additive manufacturing / 3D printing in ergonomic aspects of product design: A systematic review. Appl Ergon. 2021;97:103528. doi:10.1016/j.apergo.2021.103528

[47] Colibrium Additive GE Aerosapce, Spectra H. 2024 [cited 2024 Sep 20]. Available from https://www.colibriumadditive.com/printers/eb-pbf-printers/spectra-h.

[48] Kourra N, Warnett JM, Attridge A, et al. Computed tomography metrological examination of additive manufactured acetabular hip prosthesis cups. Manuf. 2018;22:146–152. doi:10.1016/j.addma.2018.04.033

[49] Wang P, Tan X, Nai MLS, et al. Spatial and geometrical-based characterization of microstructure and microhardness for an electron beam melted Ti–6Al–4 V component, Mater Des. 2016;95:287–295.

[50] Pham MT, Yeo SH, Teo TJ, et al. Design and optimization of a three degrees-of-freedom spatial motion compliant parallel mechanism with fully decoupled motion characteristics. J Mech Robot. 2019;11(5):051010–8. doi:10.1115/1.4043925

[51] Zhu J, Zhou H, Wang C, et al. A review of topology optimization for additive manufacturing: status and challenges. Chinese J Aeronaut. 2021;34:91–110. doi:10.1016/j.cja.2020.09.020

[52] Yusaku M, Kosuke K, Wang P, et al. A high quality Alloy718 powder for powder Bed fusion additive manufacturing. Hitachi Metal Tech Rev. 2020;36:48–57.

[53] Kotzem D, Arold T, Niendorf T, et al. Influence of specimen position on the build platform on the mechanical properties of as-built direct aged electron beam melted inconel 718 alloy. Mater Sci Eng. 2020;A772:138785. doi:10.1016/j.msea.2019.138785

[54] Zhai W, Wang P, Ng FL, et al. Hybrid manufacturing of γ-TiAl and Ti–6Al–4 V bimetal component with enhanced strength using electron beam melting. Compos Part B: Eng. 2020: 108587.

[55] Juechter V, Franke MM, Merenda T, et al. Additive manufacturing of Ti-45Al-4Nb-C by selective electron beam melting for automotive applications. Addi Manuf. 2018;22:118–126.

[56] Raghavan N, Dehoff R, Pannala S, et al. Numerical modeling of heat-transfer and the influence of process parameters on tailoring the grain morphology of IN718 in electron beam additive manufacturing. Acta Mater. 2016;112:303–314. doi:10.1016/j.actamat.2016.03.063

[57] Wang P, Nai MLS, Ng FL, et al. Revealing mechanisms underlying powder reusability of Ti-48Al-2Cr-2Nb intermetallic in electron beam powder bed fusion process. Addit Manuf. 2022;59:103155.

[58] Prabhakar P, Sames WJ, Dehoff R, et al. Computational modeling of residual stress formation during the electron beam melting process for inconel 718. Addit Manuf. 2015;7:83–91.

[59] Al-Bermani S, Blackmore M, Zhang W, et al. The origin of microstructural diversity, texture, and mechanical properties in electron beam melted Ti-6Al-4V. Metall Mater Trans A. 2010;41(13):3422–3434. doi:10.1007/s11661-010-0397-x

[60] Hinojos A, Mireles J, Reichardt A, et al. Joining of inconel 718 and 316 stainless steel using electron beam melting additive manufacturing technology. Mater Des. 2016;94:17–27.

[61] Yamanaka K, Saito W, Mori M, et al. Preparation of weak-textured commercially pure titanium by electron beam melting. Addit Manuf. 2015;8:105–109.

[62] Grubova IY, Kozadaeva M, Volkova AP, et al. Process window for electron beam melting of Ti–42Nb wt.%. J Mater Res Technol. 2023;25:4457–4478. doi:10.1016/j.jmrt.2023.06.234

[63] Yang K, Wang J, Tang H, et al. Additive manufacturing of in-situ reinforced Ti–35Nb–5Ta–7Zr (TNTZ) alloy by selective electron beam melting (SEBM). J Alloys Compd. 2020;826:154178. doi:10.1016/j.jallcom.2020.154178

[64] Kenevisi MS, Lin F. Effect of powder characteristics on relative density and porosity formation during electron beam selective melting of Al2024 aluminum alloy. J Manuf Sci Eng. 2023;145(5):054501. doi:10.1115/1.4056665

[65] Lodes MA, Guschlbauer R, Körner C. Process development for the manufacturing of 99.94% pure copper via selective electron beam melting. Mater Lett. 2015;143:298–301.

[66] Momeni S, Guschlbauer R, Osmanlic F, et al. Selective electron beam melting of a copper-chrome powder mixture. Mater Lett. 2018;223:250–252.

[67] Wang P, Huang P, Ng FL, et al. Additively manufactured CoCrFeNiMn high-entropy alloy via pre-alloyed powder. Mater Des. 2019;168:107576.

[68] Cagirici M, Wang P, Ng FL, et al. Additive manufacturing of high-entropy alloys by thermophysical calculations and in situ alloying. J Mater Sci Technol. 2021;94:53–66. doi:10.1016/j.jmst.2021.03.038

[69] Gokcekaya O, Ishimoto T, Todo T, et al. Influence of powder characteristics on densification via crystallographic texture formation: pure tungsten prepared by laser powder bed fusion. Addit Manuf Lett. 2021;1:100016. doi:10.1016/j.addlet.2021.100016

[70] Niu P, Li R, Gan K, et al. Manipulating stacking fault energy to achieve crack inhibition and superior strength–ductility synergy in an additively manufactured high-entropy alloy. Adv Mater. 2024;36:2310160. doi:10.1002/adma.202310160

[71] Cagirici M, Guo S, Ding J, et al. Additive manufacturing of high-entropy alloys: current status and challenges. Smart Mater Manuf. 2024;2:100058. doi:10.1016/j.smmf.2024.100058

[72] Altair. (2019). Generative design and topology optimization for AM by Altair, https://cdn2.hubspot.net/hubfs/47251/Altair_Generative_Design_Report.pdf.

[73] Vaneker T, Bernard A, Moroni G, et al. Design for additive manufacturing: framework and methodology. CIRP Ann 2020;69(2):578–599. doi:10.1016/j.cirp.2020.05.006